Inductively-Tuned K/Ka Band RF MEMS Capacitive Switches

Hao Wei[1, *], Shiwang Jia[1], and Zhongliang Deng[2]

Abstract—This paper designs, fabricates, and analyzes an inductively-tuned K/Ka band RF MEMS (Radio frequency micro-electro-mechanical-systems) capacitive switches. The MEMS switch employs a defect ground structure (DGS) and an air bridge. Two different MEMS switches, one with air bridges and the other not, are designed. Surface current distribution results of MEMS switches in different states are simulated and discussed. A novel actuation voltage's calculation approach of MEMS switch is proposed. Measured results indicate that the type MEMS switch's actuation voltage is 20 V. For the MEMS switch without air bridges, the isolation is more than 15 dB from 12.5 to 20 GHz, and the insertion loss is less than 0.28 dB up to 20 GHz. For the MEMS switch with integrated air bridges, the isolation is more than 15 dB from 18.3 to 40 GHz, and the insertion loss is less than 0.64 dB up to 40 GHz. Circuit models and measured results of the proposed MEMS switches show good agreements. The pull-in and release time of this switch are 99 μs and 49 μs, and the lifetime of this type of switch is more than three million.

1. INTRODUCTION

RF MEMS switches play a key role in application of reconfigurable communication [1–3]. In the application, RF performance and mechanical behavior of MEMS switches are highly regarded for the devices designed [4].

Many MEMS switches with excellent performance have been proposed, with solutions taking advantage of material properties [5, 6], series-shunt switches combination [7], MEMS bridge topology optimization [8], and geometric design [9]. However, there is an obvious disadvantage of these methods, and the mechanical properties of MEMS switch are changed when the operating frequency is changed. Every change in the system mechanics requires repetitions of reliability and qualification tests, making the development very cost intensive [10].

This paper provides a better solution of the frequency tuning of MEMS capacitive switches, and it is easy to implement without changing the mechanics of the device. Some approaches have been reported, including the MEMS switch with integrated inductive loads [10], short high impedance section of transmission line between the MEMS beam and ground plane [11], and forming the equivalent inductance by DGS [12].

The MEMS switch with integrated air bridges to tune the shunt inductance and center frequency is introduced. In this paper, the beam's size is changed from what we proposed before in [13].

Simulated and measured results both show that DGS covered with air bridges can change the shunt inductances of the MEMS shunt switches. Meanwhile, MEMS switches can obtain a high isolation in a wider frequency range and less insertion loss.

2. DESIGN OF INDUCTIVELY-TUNED K/KA BAND MEMS SWITCHES

2.1. Physical Dimension of the Proposed Switch

The MEMS beam structure is shown in Fig. 1, and compared with the beam structure in [13], the sizes of the center plate and elliptic ring are larger. The displacements and Von-Mises stresses of different beams loaded same stresses are simulated, as illustrated in Fig. 2. From the comparison of different pictures, we can find that the stress of beam #1 is evenly distributed. Meanwhile, beam #1 has a better stability.
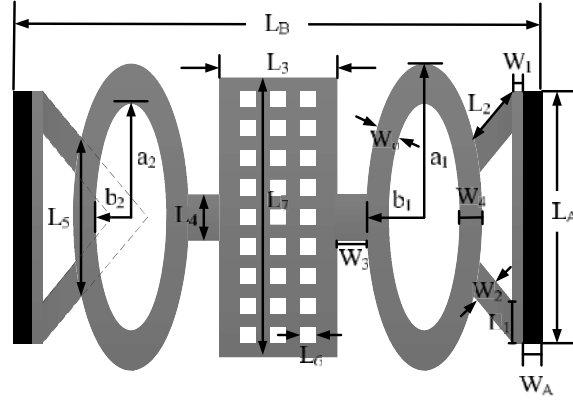

Figure 1. Optimization of the MEMS switch beam in [12].
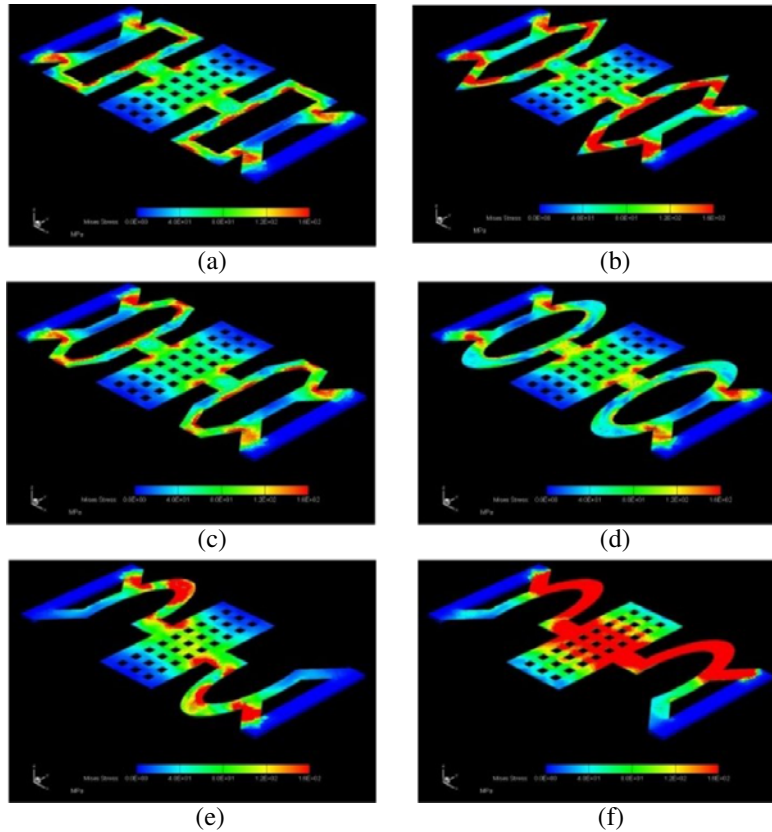

(a) (b)

(c) (d)

(e) (f)

Figure 2. Simulation results of the Von Mises stresses of different beams loaded stresses.

The MEMS switches are fabricated on high-resistance silicon (a dielectric constant ε_r of 11.9, thickness of 400 μm, dielectric loss tangent of 0.0025). Fig. 3 shows the top view of the proposed switch with DGS; the gray denotes the metal (Au); the black is the substrate; and the orange is the MEMS beam (Au). The inline MEMS shunt switch is as a part of the transmission line.
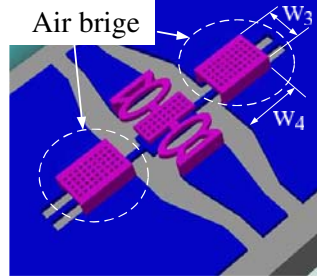

Figure 3. The MEMS switch with integrated air bridges.

The size of the waveguide port is 64/94/64 μm (G/S/G), and in the area of the MEMS switch, the size is increased to 99/170/99 μm. The center bottom ($\sim$300 $\times$ 200 μm^2) is located between two short stubs connected to ground. The parameters of l_1, (l_2, l_3), (l_4, l_5, l_6 and l_7), (a_1, b_1), (a_2, b_2) are the width of short stub, the width and length of DGS, sizes for different parts of the MEMS switch, the sizes of release holes, the long axis and short axes of an elliptical inner ring, the long axis and short axes of an elliptical outer ring, respectively. The values of l_1, l_2, l_3, l_4, l_5, l_6, l_7, a_1, b_1, a_2, b_2, w_1, and w_2 are 20, 40, 296, 20, 29, 15, 10, 75, 25, 104, 40, 89, and 190 μm, respectively.

Figure 3 shows the MEMS switch with integrated air bridges, and air bridges are both at the top of DGS. (w_3 and w_4) are the width and length of air bridges.

2.2. Calculated Model of the MEMS Switch's Pull-in Voltage

In the traditional calculated model of MEMS switch's actuation voltage, a relatively large error is caused because the fringing capacitance is always ignored. To decrease the error, a calculated approach of the actuation voltage is proposed in this paper. In the proposed calculated approach, the up-state capacitance is modeled as a filled microstrip line filled with air and dielectric.

For the MEMS switch, the up-state capacitance consists of air capacitance C_{air} and dielectric capacitance C_{die}. As shown in Fig. 4, the MEMS switch can be shown in two cross sections, which are AA' and BB', respectively.

The value of the gap g is much less than w and W, so the up-state capacitance C_{up} is given by Equations (1)$\sim$(7) [11].

$$Z_{ml1} = \frac{120\pi}{\sqrt{\varepsilon_{effml1}}\left[w/g + 1.393 + 0.667\ln(w/g + 1.444)\right]} = \frac{1}{cC_{p1}} \tag{1}$$

$$\varepsilon_{effml1} = \frac{\varepsilon_r + 1}{2} + \frac{\varepsilon_r - 1}{2}\sqrt{1 + 12w/g} \tag{2}$$

$$Z_{ml2} = \frac{120\pi}{\sqrt{\varepsilon_{effml2}}\left[W/g + 1.393 + 0.667\ln(W/g + 1.444)\right]} = \frac{1}{cC_{p2}} \tag{3}$$

$$\varepsilon_{effml2} = \frac{\varepsilon_r + 1}{2} + \frac{\varepsilon_r - 1}{2}\sqrt{1 + 12W/g} \tag{4}$$

$$C_{air} = C_{p1}W + C_{p2}w - \varepsilon_0 wW/g \tag{5}$$

$$C_{die} = \frac{\varepsilon_0 wW}{t_d/\varepsilon_r + g} \tag{6}$$

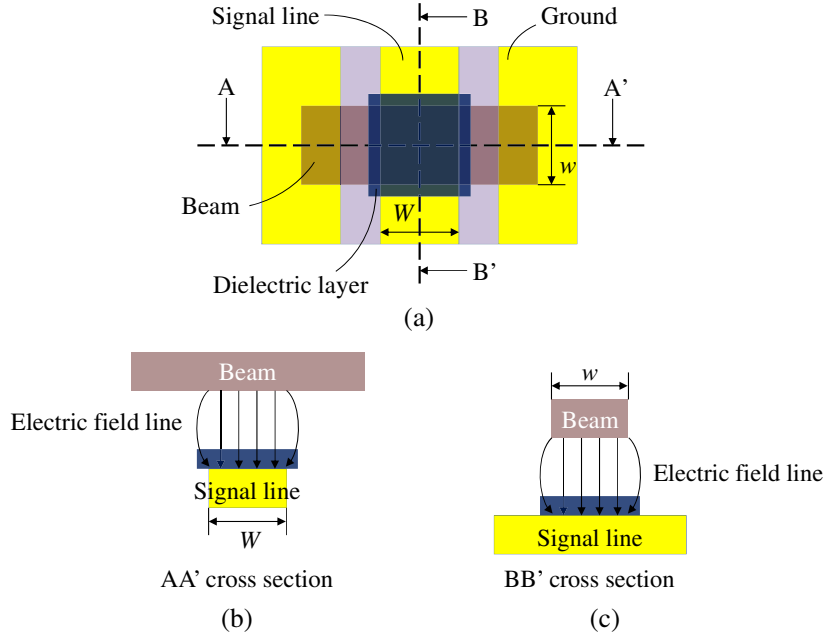$$C_{up} = \frac{C_{air}C_{die}}{C_{air} + C_{die}} \tag{7}$$

Figure 4. The topological structure of the beam. (a) Top view of the MEMS switch; (b) Side view of the bridge from side AA'; (c) Side view of the bridge from side BB'.

where the parameters of (Z_{ml1}, Z_{ml2}), $(\varepsilon_{effml1}, \varepsilon_{effml2})$, and (C_{p1}, C_{p2}) are the characteristic impedances, equivalent dielectric constants, and capacitances in per unit length of microstrip line in Fig. 4(b) and Fig. 4(c), respectively. c is the velocity of light in free space, ε_0 the effective dielectric constant in free space, and ε_r the dielectric constant of dielectric layer between the conductors.

In [16], the static capacitances of the MEMS switch with different sizes are given as shown in Table 1. From Table 1, the fringing capacitance C_f of the MEMS switch is decreased along with the reduction of gap g.

Table 1. Simulated static capacitance of a MEMS switch (the beam's length is $300\,\mu$m, the beam's thickness is $2\,\mu$m, the thickness of the dielectric layer is $0.15\,\mu$m , and the dielectric constant of dielectric layer between the conductors ε_r is 7.6) [16].

$w \times W\,(\mu\mathrm{m}^2)$	$g(\mu\mathrm{m})$	$C_u(\mathrm{fF})$	$C_{pp}(\mathrm{fF})$	$C_f(\mathrm{fF})$	$C_f/C_{pp}(\%)$
40×100	4	13.8	8.8	5	57%
80×100	4	23.4	17.6	5.8	33%
140×160	4	59.2	49.3	9.9	20%
40×100	1.5	29.8	23.2	6.5	28%
80×100	1.5	55.6	46.6	9	19%

Table 2 shows the compared results between the up-state capacitance in [16] and the up-state capacitance using this proposed calculated model. In this paper, the proposed MEMS switch's gap is $1.5\,\mu$m, and the pole's area is more than $80 \times 100\,\mu$m^2, so this proposed calculated model of pull-in voltage is adopted for the proposed MEMS switch.

For this MEMS switch, different calculated results of the pull-in voltages are shown in Fig. 5. Compared with the error between the calculated results ignoring the fringing capacitance and the simulated results using FEM software, the error caused by the calculated results using the proposed model is smaller.

Table 2. The calculated error of the up-state capacitance using this proposed calculated model.

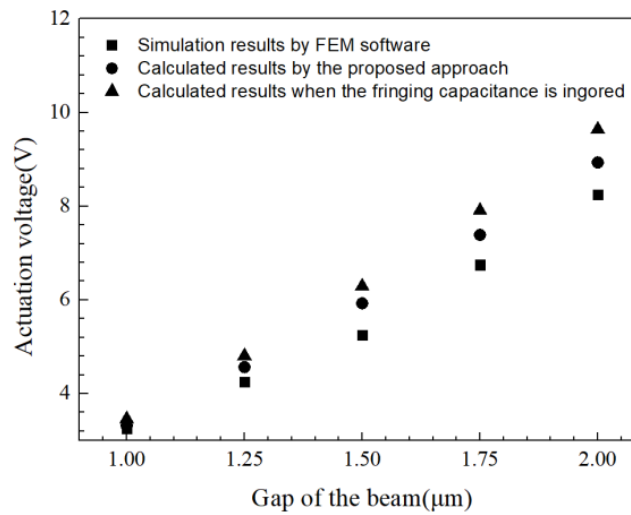| $w \times W$ (μm^2)	g (μm)	C_{ui} (fF)[16]	C_{pp} (fF)	C_{u2} (fF)	error (%) $(C_{u1}\text{-}C_{u2})/C_{u1}$
40×100	4	13.8	8.8	12.7	8%
80×100	4	23.4	17.6	23.1	1.3%
140×160	4	59.2	49.3	59.3	0.2%
40×100	1.5	29.8	23.2	27.8	6.7%
80×100	1.5	55.6	46.6	52.9	4.9%

Figure 5. Different calculated results of the actuation voltages.

Table 3 gives the actuation voltage's calculated errors of different calculated approaches. The simulation results by FEM software are as the reference standard. Compared to the traditional calculated approach which ignores the fringing capacitance, the proposed approach's calculated error is smaller.

Table 3. The actuation voltage's calculated errors of different calculated approach.

g (μm)	FSR (V)	PAR (V)	TAR [16] (V)	Error1*	Error2*
2	8.25	8.94	9.64	8.36%	16.84%
1.75	6.75	7.39	7.91	9.48%	17.19%
1.5	5.25	5.93	6.29	12.95%	19.81%
1.25	4.25	4.56	4.80	7.29%	12.94%
1	3.25	3.32	3.46	2.1%	6.46%

*FSR = FEM software's results
*PAR = the proposed approach's results
*TAR = the traditional approach's results
*Error1 = (PAR-FSR)/FSR × 100%
*Error2 = (TAR-FSR)/FSR × 100%

2.3. Surface Current Distribution of MEMS Switches

As shown in Fig. 6, there are significant differences in surface current distribution of different MEMS switches. When the MEMS switch without the air bridge is in up state, the current flows around the slots of DGS, and simulation results of Mag Jsurf [A_per_m] by HFSS software for the slots area are larger than 500. Fig. 6(c) shows simulation results of the MEMS switch with integrated air bridges. DGS is covered with air bridges, and only a small amount of current flows into the DGS when the MEMS switch is in up state. When the MEMS switch is in down state, Fig. 6(b) and Fig. 6(d) show that the currents flow into the ground as MEMS switches work around their resonant frequencies.
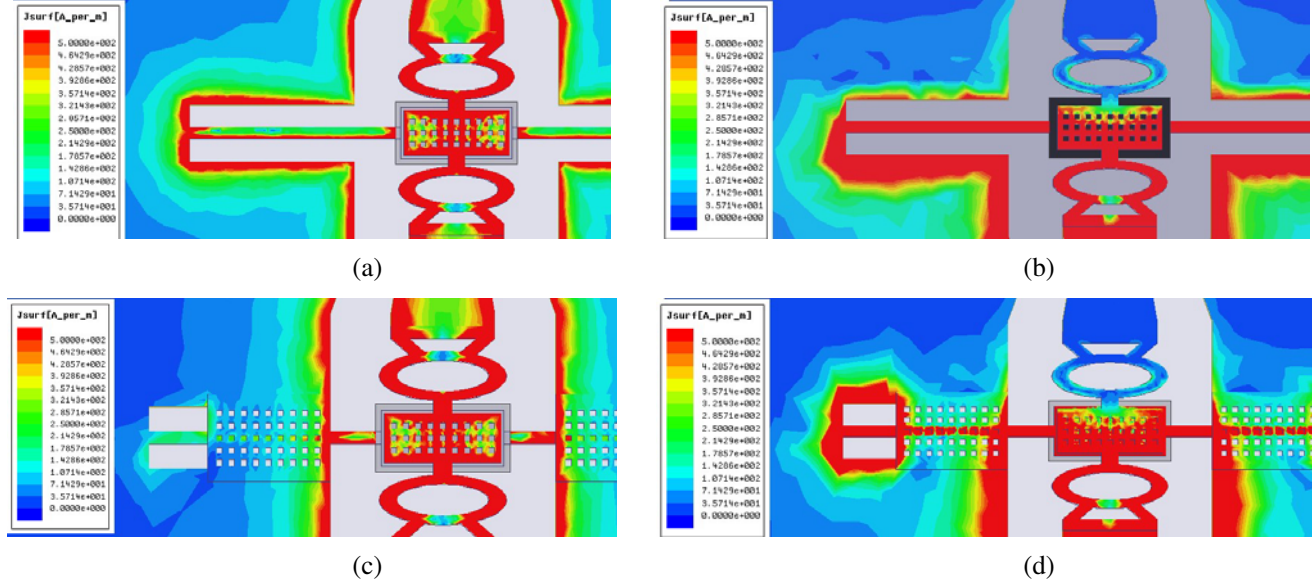

(a)   (b)

(c)   (d)

Figure 6. Surface current distribution results of MEMS switches, (a) the MEMS switch with DGS is in up state; (b) the MEMS switch with DGS is in down state; (c) the MEMS switch with integrated air bridges is in up state; (d) the MEMS switch with integrated air bridges is in down state.

The air bridge's model is as shown in Fig. 7. The value of gap (g) is much smaller than the width (w_4), so the capacitance (C_0) can be calculated by Equations (1)$\sim$(7).
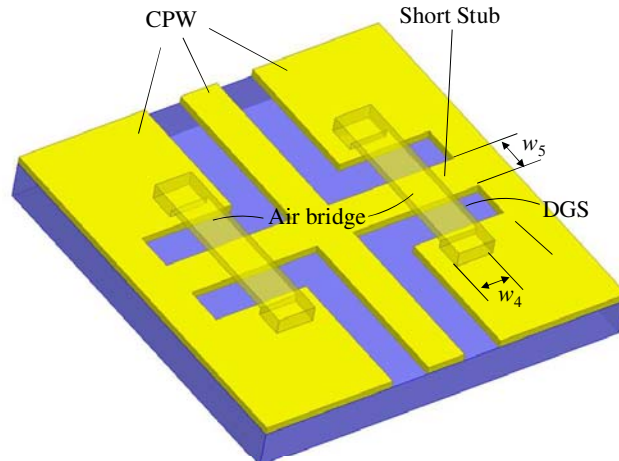

Figure 7. An shunt capacitance between the air bridge and short stub.
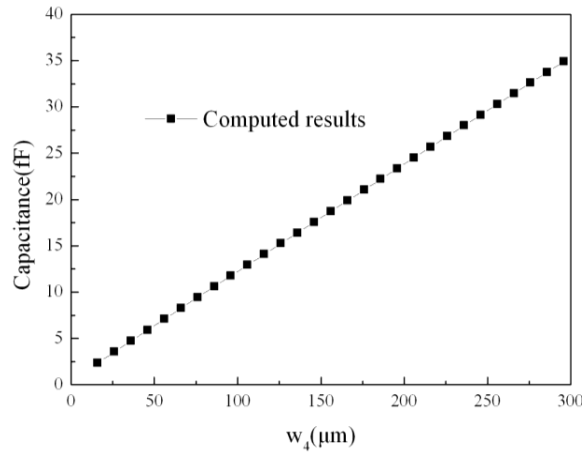
Figure 8. The capacitance (C_0) versus the width (w_4) of the air bridge.
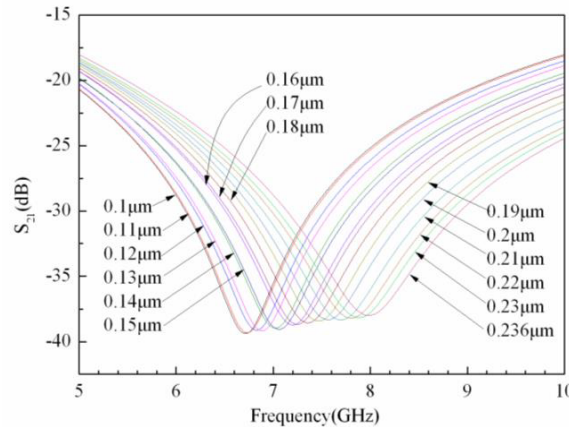

Figure 9. The width (w_4) versus the MEMS switch's S_{21}.

When DGS is covered with air bridges, Fig. 8 shows the relationship between the shunt capacitance C_0 and width (w_4) of the air bridge without the release holes. As w_4 gets larger, the value of C_0 is increased. Fig. 9 and Fig. 10 show the value of w_4 versus the center frequency and shunt inductance L_0, respectively.

We can find that the value of the inductance and center frequency are inversely proportional to the value of w_4. For the proposed switch, the values of w_3, w_4, and w_5 are 140, 200, and 20 μm, respectively.

3. FABRICATION PROCESS FLOW

The substrate uses high resistance silicon with a thickness of 0.4 mm, and a layer of Au is located in the back of the substrate [Fig. 11(a)]. As an isolator, SiO_2 is obtained by thermal oxidation [Fig. 11(b)]. The layer of SiCr, as a high resistance dc-bias line, is deposited over a layer of SiO_2 [Fig. 11(c)]. The layer of SiCr is covered with a layer of SiN [Fig. 11(d)]. The center line of CPW is connected to the dc ground pad through a bias high resistance line. Each switch has a separate high resistance dc-bias line for independent control. A thinner layer of Au is sputtered and patterned, which is used to form transmission lines structures and the pads, and some regions of the lines are electroplated [Fig. 11(e)]. 0.15 μm thickness of Si_3N_4 is formed by plasma enhanced chemical vapor deposition (PECVD), and the layer is patterned on the top of the bottom electrode [Fig. 11(f)]. The thickness of the sacrificial layer is about 2 μm [Fig. 11(g)]. The anchors and the beam are formed by the electroplating technology. The
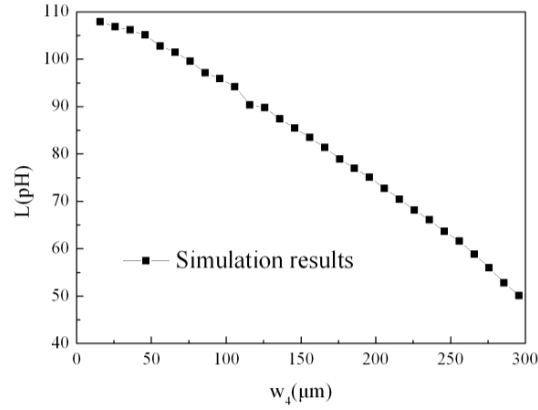
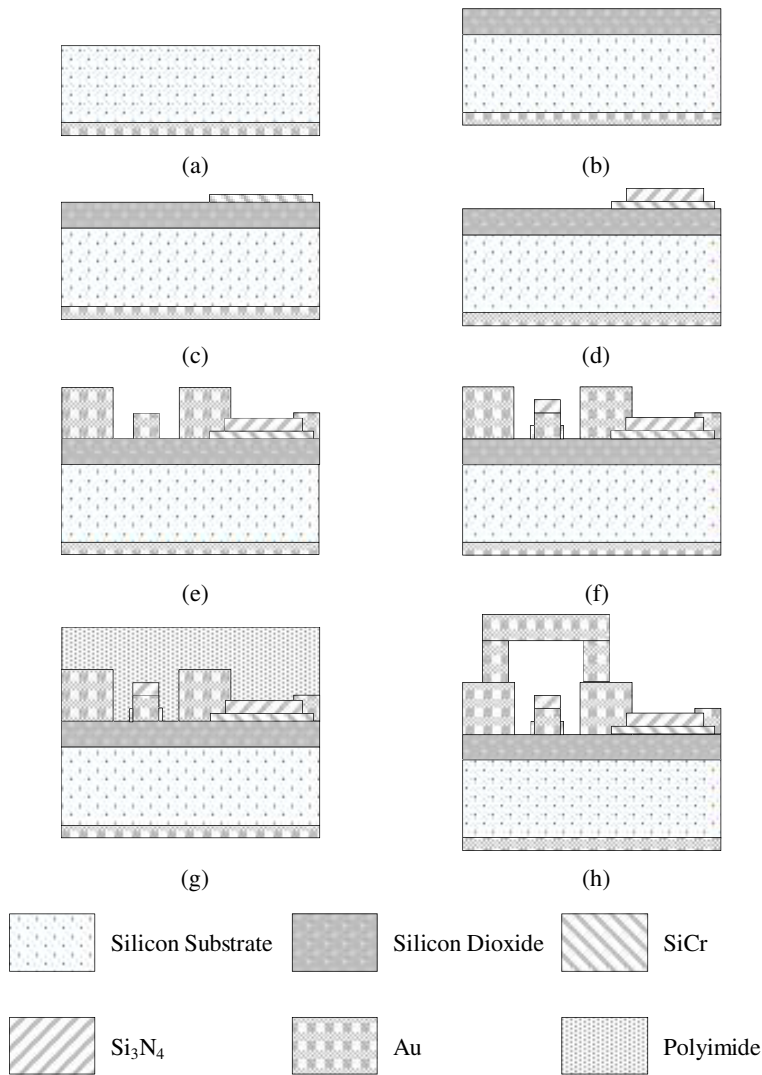**Figure 10.** The width (w_4) versus the shunt inductance L_0.

Figure 11. Cross section of MEMS switches (a) after RCA cleaning, (b) after oxidation, (c) after patterning of high resistance dc-bias lines, (d) after patterning of the layer of Si_3N_4, (e) after patterning of CPW lines, (f) after patterning of the layer of Si_3N_4, (g) spinning of polyimide to form the sacrificial layer (h) patterning of the layer of Au to form MEMS beams and anchors, removal of the sacrificial layer.

thickness of the beam is about 1 μm, and the sacrificial layer is released by the technology of supercritical dry release finally [Fig. 11(h)].

Figure 12(a) shows the micrograph of the fabricated MEMS switches without air bridges. Fig. 12(b) shows the micrograph of the fabricated MEMS switches with integrated air bridges.
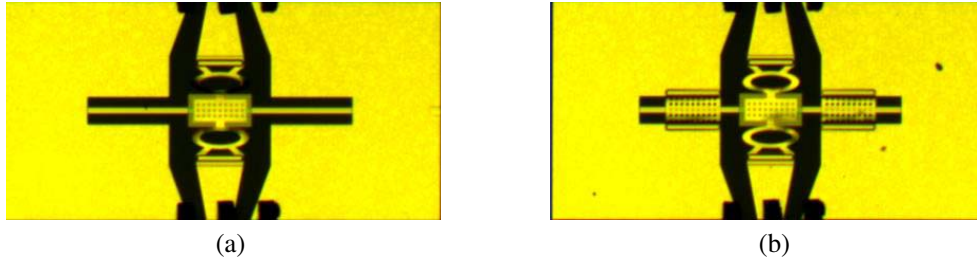

(a)   (b)

Figure 12. Micrograph of fabricated MEMS switches. (a) The MEMS switch without the air bridge. (b) The MEMS switch with integrated air bridge.

4. MEASUREMENT AND ANALYSIS

4.1. Measurement

The unpackaged devices are measured in standard laboratory environment. S_{21} parameters (insert loss and insolation) of the devices are measured by the Vector Network Analyzer (R&S ZVA50), two gold ACP-A-GSG-150 probes, and a probe table (Cascade Summit 11000B-M). The sweep frequency is from 100 MHz to 40 GHz.

Figure 13 shows S_{21} of measured results and circuit models of MEMS switches. Measured results indicate that for the switch without air bridges, the isolation is more than 15 dB at $12.5 \sim 20$ GHz when the voltage is ~ 10 V; the maximum isolation is 25.3 dB at the resonant frequency of 15.54 GHz; and the insertion loss is less than 0.28 dB up to 20 GHz. However, in 40 GHz, the loss of this MEMS switch is nearly 1 dB.
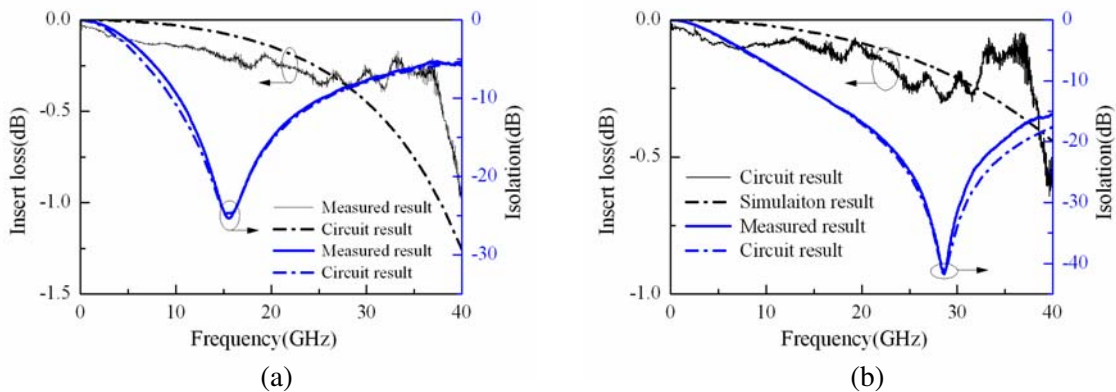

(a)   (b)

Figure 13. S_{21} of the proposed MEMS switches (a) S_{21} of the circuit model and measured results of the MEMS switch without air bridges. (b) S_{21} of the circuit model and measured results of the MEMS switch with integrated air bridges.

Compared with the switch without air bridges, the switch with integrated air bridge has a wider stopband and less insertion loss. The isolation is more than 15 dB at $18.3 \sim 40$ GHz when the voltage is ~ 20 V. The maximum isolation is 41.7 dB at the resonant frequency of 28.63 GHz, and the insertion loss is less than 0.64 dB up to 40 GHz. From Fig. 13, we find that the insert loss of the MEMS integrated with the air bridges is smaller.

4.2. Switching Time and Lifecycles

The beams of these MEMS switches are same, and one of the MEMS switch's switching time is measured on wafer in a clean room. The switching time and life cycles are measured by cascade probe station, function generator, oscilloscope, and detector. The measured results of pull-in and release times are as shown in Fig. 14. The red solid line represents the MEMS switch's RF out power detected by detector, and the blue solid line represents the square wave DC bias voltage for the MEMS switch. When the MEMS switch is actuated by a voltage of $\sim 20\,\mathrm{V}$, the switch is pulled down to contact with the dielectric layer, and it changes the on-state to the off-state. The switching time is $99\,\mathrm{\mu s}$. On the contrary, when the pull-in voltage is $0\,\mathrm{V}$, the fixed-fixed beam is released, and the MEMS switch changes its off-state to the on-state. The switching time is $46\,\mathrm{\mu s}$. The frequency of the function generator is $1\,\mathrm{KHz}$, and the duty cycle of the voltage square wave is 50%. The lifetime of the MEMS switch without invalid is more than 3.6×10^6 cycle.
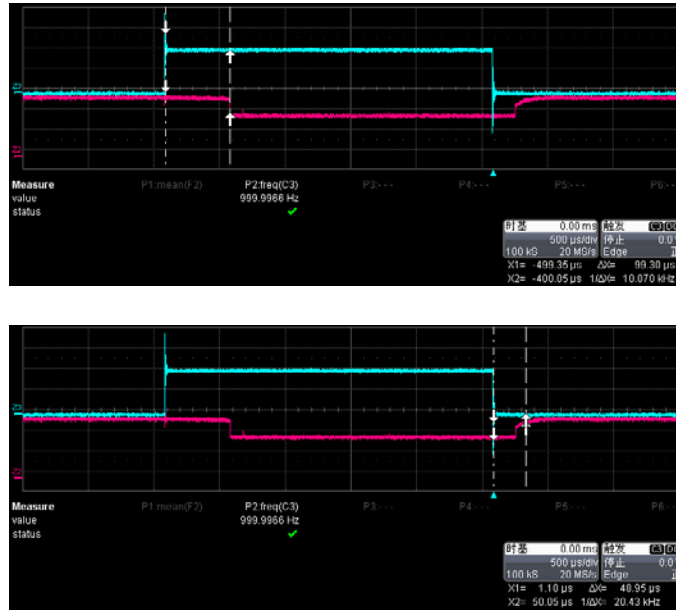

Figure 14. The measured on/off time of the proposed RF MEMS switch.

5. CONCLUSION

Inductively-tuned RF MEMS switches with DGS and air bridges are proposed, and DGS is covered with air bridges. The MEMS switches are designed, fabricated, measured, and analyzed. The relationship between the sizes of air bridges and the equivalent inductances is analyzed. Simulated results show that the sizes of air bridges are related to the change of shunt inductances and shunt capacitances. Measured results indicate that compared with the MEMS switch without air bridges, the MEMS switch with air bridge exhibits a smaller insert loss in the high frequency, and its down-state resonant frequency is higher.

REFERENCES

1. Tahir, F. A. and H. Aubert, "Equivalent electrical circuit for designing MEMS-controlled reflectarray phase shifters," *Progress In Electromagnetics Research*, Vol. 100, 1–12, 2010.
2. Pourziad, A., S. Nikmehr, and H. Veladi, "A novel multi-state integrated RF MEMS switch for reconfigurable antennas applications," *Progress In Electromagnetics Research*, Vol. 139, 389–406, 2013.

3. Martinez-Lopez, R., J. Rodriguez-Cuevas, A. E. Martynyuk, and J. I. Martinez-Lopez, "An active ring slot with RF MEMS switchable radial stubs for reconfigurable frequency selective surface applications," *Progress In Electromagnetics Research*, Vol. 128, 419–440, 2012.

4. Jia, S. and F. Zhao, "Design of a MEMS reconfigurable group delay equalizer," *Radio Engineering*, Vol. 48, No. 4, 208–313, 2018.

5. Sharma, P., J. Perruisseau-Carrier, C. Moldovan, and A. M. Ionescu, "Electromagnetic performance of RF NEMS graphene capacitive switches," *IEEE Transactions on Nanotechnology*, Vol. 13, No. 1, 70–79, Jan. 2014, doi: 10.1109/TNANO.2013.2290945.

6. Fernandez-Bolanos Badia, M., E. Buitrago, and A. M. Ionescu, "RF MEMS shunt capacitive switches using AlN compared to Si_3N_4 dielectric," *Journal of Microelectromechanical Systems*, Vol. 21, No. 5, 1229–1240, Oct. 2012, doi: 10.1109/JMEMS.2012.2203101.

7. Singh, T., "Design and finite element modeling of series-shunt configuration based RF MEMS switch for high isolation operation in K-Ka band," *Journal of Computational Electronics*, Vol. 14, No. 1, 167–179, Mar. 2015, doi: 10.1007/s10825-014-0636-2.

8. Angira, M., G. M. Sundaram, and K. J. Rangra, "A novel approach for low insertion loss, multi-band, capacitive shunt RF-MEMS switch," *Wireless Personal Communications*, Vol. 83, No. 3, 2289–2301, Aug. 2015, doi: 10.1007/s11277-015-2521-0.

9. Philippine, M. A., H. Zareie, O. Sigmund, G. M. Rebeiz, and T. W. Kenny, "Experimental validation of topology optimization for RF MEMS capacitive switch design," *Journal of Microelectromechanical Systems*, Vol. 22, No. 6, 1296–1309, Dec. 2013, doi: 10.1109/JMEMS.2013.2283241.

10. Kaynak, M., et al., "Packaged BiCMOS embedded RF-MEMS switches with integrated inductive loads," *2012 IEEE MTT-S International Microwave Symposium Digest (MTT)*, 1–3, Montreal, QC, Canada, 2012, doi: 10.1109/MWSYM.2012.6259417.

11. Muldavin, J. B. and G. M. Rebeiz, "High-isolation inductively-tuned X-band MEMS shunt switches," *2000 IEEE MTT-S International Microwave Symposium Digest*, Vol. 1, 169–172, Boston, MA, USA, 2000, doi: 10.1109/MWSYM.2000.860923.

12. Zhang, N., Z. Deng, and F. Sen, "CPW tunable band-stop filter using hybrid resonator and employing RF MEMS capacitors," *IEEE Transactions on Electron Devices*, Vol. 60, No. 8, 2648–2655, Aug. 2013, doi: 10.1109/TED.2013.2270359.

13. Deng, Z. L., H. Wei, S. Fan, and J. Gan, "Design and analysis a novel RF MEMS switched capacitor for low pull-in voltage application," *Microsyst. Techn.*, 1–9, 2015, doi: 10.1007/s00542-015-2604-6.

14. Hanna, V. F., "Parameters of coplanar diretional couplers with lower ground plane," *15th European Microwave Conference, 1985*, 820–825, Paris, France, 1985, doi: 10.1109/EUMA.1985.333579.

15. Ghione, G. and C. Naldi, "Parameters of coplanar waveguides with lower ground plane," *Electronics Letters*, Vol. 19, No. 18, 734–735, Sep. 1983, doi: 10.1049/el:19830500.

16. Rebeiz, G. M., *RF MEMS: Theory, Design, and Technology*, John Wiley & Sons, 2004.